OPEN ACCESS
IOP Publishing
Journal of Physics: Condensed Matter
J. Phys.: Condens. Matter **37** (2025) 045802 (12pp)
https://doi.org/10.1088/1361-648X/ad8c0a

Magnetic order in nanogranular iron germanium ($Fe_{0.53}Ge_{0.47}$) films

Ruthi Zielinski[1], Nhat Nguyen[1], Bryce Herrington[1], Amir Tarkian[1], Omar Taha[1], Wai Kiat Chin[1], Ather Mahmood[1], Xiaoqian Chen[2], Christoph Klewe[3], Padraic Shafer[3], Jim Ciston[4], Paul Ashby[4], Claudio Mazzoli[2] and Robert Streubel[1,5,*]

[1] Department of Physics and Astronomy, University of Nebraska-Lincoln, Lincoln, NE 68588, United States of America
[2] National Synchrotron Light Source II, Brookhaven National Laboratory, Upton, NY 11973, United States of America
[3] Advanced Light Source, Lawrence Berkeley National Laboratory, Berkeley, CA 94720, United States of America
[4] Molecular Foundry, Lawrence Berkeley National Laboratory, Berkeley, CA 94720, United States of America
[5] Nebraska Center for Materials and Nanoscience, University of Nebraska-Lincoln, Lincoln, NE 68588, United States of America

E-mail: streubel@unl.edu

Received 28 June 2024, revised 4 October 2024
Accepted for publication 28 October 2024
Published 12 November 2024

Abstract

We study the effect of strain on the magnetic properties and magnetization configurations in nanogranular Fe_xGe_{1-x} films ($x = 0.53 \pm 0.05$) with and without B20 FeGe nanocrystals surrounded by an amorphous structure. Relaxed films on amorphous silicon nitride membranes reveal a disordered skyrmion phase while films near and on top of a rigid substrate favor ferromagnetism and an anisotropic hybridization of Fe *d* levels and spin-polarized Ge *sp* band states. The weakly coupled topological states emerge at room temperature and become more abundant at cryogenic temperatures without showing indications of pinning at defects or confinement to individual grains. These results demonstrate the possibility to control magnetic exchange and topological magnetism by strain and inform magnetoelasticity-mediated voltage control of topological phases in amorphous quantum materials.

Supplementary material for this article is available online

Keywords: amorphous film, topological magnetism, magnetic moment, strain, magnetic imaging, x-ray photon correlation spectroscopy

* Author to whom any correspondence should be addressed.

1. Introduction

Coordination and strain govern the hybridization of electron orbitals in solid-state materials and can fundamentally affect electronic and magnetic properties of functional materials. Systems with inversion symmetry breaking and dominant Dzyaloshinskii–Moriya interaction [1, 2], such as cubic B20 FeGe [3–9], stabilize a variety of topological phases, including spin knots commonly referred to as hopfions [8–11], that may find application in racetrack memory [12–14], spin resonators [15, 16], magnetic tunnel junctions [17, 18], topological magnonics [19, 20], or physical reservoir computing [21, 22]. For either application, a magnetoelasticity-mediated voltage control of magnetic exchange, magnetic anisotropy, saturation magnetization, and topological phases is desirable. The latter aspiration has mainly driven research in two-dimensional van-der-Waals materials [23–28]. However, recent advances in creating amorphous topological insulators [29–31], amorphous topological superconductors [32], amorphous topological metals [33], amorphous spin liquids [34, 35], and amorphous topological magnetic systems [36, 37] demonstrate that these considerations go beyond lattice symmetry. The structural and chemical disorder, that can be tuned by deposition temperature and rate [38–40] and post-growth annealing [41–43], cause an inequivalency of sites and a distribution of magnetic exchange, moment, and single-ion anisotropy [44]. The resulting exchange interactions can be much stronger than in crystals [45] and change its sign [46, 47], promoting spin frustration and the formation of spin glasses and topological phases [45].

Strain-induced modifications to the orbital hybridization enabled the tuning of ferromagnetic resonances [48, 49] and magnetic exchange in multilayers with perpendicular magnetic anisotropy [50] as well as the manipulation of topological states using, e.g. surface acoustic waves [51–55]. Strain is also envisioned to alter the topology of magnetic states [56–60]. Isotropic pressure in itinerant metals allowed for increasing the delocalization of electrons, weakening magnetism [61, 62], and decreasing transition temperatures [63, 64]. By extension, films grown on rigid substrates and free-standing membranes are likely to yield distinct physical properties due to varying deposition conditions (thermal conductance) and strain relaxation, and to provide a prototypical system to demonstrate the strain control of magnetic exchange to promote topological magnetism in films.

Here, we demonstrate the influence of coordination and strain on the magnetic properties of nanogranular Fe_xGe_{1-x} films ($x = 0.53 \pm 0.05$) with and without B20 FeGe nanocrystals embedded in an amorphous structure. The composition is chosen to promote the formation of helical spins and topological magnetic states [36]. The films are grown on amorphous silicon nitride wafers and membranes to showcase the differences in magnetic anisotropy, exchange, and saturation magnetization associated with strain relaxation. X-ray magnetic circular dichroism (XMCD) spectroscopy confirms the hybridization of Fe *d* levels and Ge *sp* band states by detecting an induced germanium moment and quantifying the orbital-to-spin moment ratio. Comparison with the orientation-dependent gyromagnetic ratio derived from ferromagnetic resonance (FMR) spectroscopy corroborates the effect of lateral isotropic strain and an orientation-dependent spin mixing typically absent in iron compounds. Magnetic imaging reveals the formation of a disordered skyrmion phase with a feature size $\lesssim$100 nm in relaxed films on membranes while films near and on top of the rigid support are ferromagnetic. The activation and freezing temperature of weakly coupled topological states, extracted from their thermal spin fluctuations with x-ray photon correlation spectroscopy (XPCS), coincide with the temperature dependence of the magnetization configuration and the blocking temperature obtained with magnetometry.

2. Materials and methods

2.1. Synthesis

The iron germanium films were co-evaporated from standard (Ge) and high-temperature (Fe) effusion cells on amorphous silicon nitride and capped with a 10 nm-thick aluminum layer using an Octoplus 300 evaporation system (MBE Komponenten GmbH) with a vacuum base pressure $\approx 10^{-10}$ mbar. Growth rates for iron [United Minerals and Chemicals (UMC), 99.99%], germanium (UMC, 99.9999%), and aluminum (UMC, 99.9999%) were 0.09 Å s^{-1}, 0.15 Å s^{-1}, and 0.15 Å s^{-1}, respectively, with an effective deposition temperature of 300 to 320 K due to radiation heating from the effusion cells. The $4 \times (7 \pm 1)$ nm films (S6) were grown in four steps, each step having a 10 nm deposition (nominal thickness t_{set}) with a 5 min-long pause (table 1). Structural characterization, magnetometry, and FMR spectroscopy were carried out with 200 nm-thick amorphous low-stress silicon nitride films deposited by low-pressure chemical vapor deposition on 525 μm-thick silicon wafers (Rogue Valley Microdevices). Kerr and Lorentz microscopy as well as XMCD spectroscopy and coherent x-ray scattering were performed with 30 nm-thick silicon nitride membranes on 200 μm-thick silicon frames (Norcada). All samples have a lateral size of roughly (2.6×2.6) mm^2.

2.2. Chemical and structural characterization

The adhesion of individual elements during co-deposition strongly depends on the substrate, co-evaporants, deposition temperature and rate and leads to deviations of the actual film thickness and composition from their respective nominal values. The different adhesion for iron and germanium and a composition of $x = 0.53 \pm 0.05$ (Fe_xGe_{1-x}) (table 1), deviating from the nominal value $x_{set} = 0.38$ set by the individual evaporation rates, were confirmed by energy-dispersive x-ray spectroscopy using Fe *K* and Ge *K* absorption edges with an FEI Helios NanoLab 660 at the Nano-Engineering Research Core Facility at the University of Nebraska–Lincoln (Lincoln, NE). Assuming an iron adhesion of 100% and identical atomic radii for Ge (122 pm) and Fe (126 pm), the actual iron germanium

Table 1. Investigated nanogranular iron germanium (Fe_xGe_{1-x}) films with nominal composition $x_{set} = 0.38$ and thickness $t = \frac{x_{set}}{x} t_{set}$. The root mean square roughness (RMS) is measured over an area of 9 μm^2. Coordination and phase segregation affect the sample-averaged saturation magnetization $M_s(0\ K)$. The blocking temperature T_B is governed by the grain size without a noticeable dependence on the crystallinity. B20 denotes the cubic B20 crystal phase of FeGe.

	Composition x	t (nm)	RMS (nm)	Grain size (nm)	Crystal phase	M_s (kA m^{-1})	T_B (K)
S1	0.53 ± 0.05	29 ± 3	4.7	55 ± 5	B20(111), B20(200), Fe(110)	225 ± 22	24
S2	0.57 ± 0.05	27 ± 3	1.7	None	B20(200), Fe(110)	601 ± 61	None
S3	0.49 ± 0.05	62 ± 6	5.9	72 ± 10	None	250 ± 25	37
S4	0.54 ± 0.05	56 ± 5	4.9	52 ± 5		344 ± 34	33
S5	0.53 ± 0.05	7 ± 1	2.8	40 ± 10	None	174 ± 17	26
S6	0.51 ± 0.05	$4 \times (7 \pm 1)$				521 ± 53	24

film thickness was calculated as $t = \frac{x_{set}}{x} t_{set}$ and exemplarily confirmed by x-ray reflectometry (see supporting information). X-ray reflectometry was performed with a Rigaku SmartLab diffractometer equipped with a Cu-K_α radiation source at the Nebraska Center for Materials and Nanoscience (Lincoln, NE). The smaller actual film thickness and increased iron concentrtion originate from a markedly lower Ge adhesion of $A_{Ge} = \frac{t_{Ge}}{t_{Ge}^{set}} \gtrsim 50\%$. A PAN alytical Empyrean diffractometer equipped with a Cu-K_α radiation source allowed for determining the crystallographic orientation at the Nebraska Center for Materials and Nanoscience (Lincoln, NE). The resulting spectra were noise-filtered using a Savitzky–Golay filter with a 0.118° window and second-order polynomial. The topography of the iron germanium films was characterized via atomic force microscopy using a Jupiter XR Asylum Research AFM with Budget Sensors (Tap 150 Al-G) tips in tapping mode at the Molecular Foundry (LBNL, Berkeley, CA). Transmission electron microscopy and selected-area electron diffraction with a 10 μm pinhole were carried out using a 300 keV aberration-corrected transmission electron microscope (TEAM I) with a Gatan K3-IS direct electron detector operated in electron-counting mode (resolution at 3300 ×: 0.55 nm) at the Molecular Foundry (LBNL, Berkeley, CA).

2.3. Magnetic characterization

Vibrating sample magnetometry and AC susceptibility measurements with a drive amplitude 0.8 kA m^{-1} at 4 kHz were performed with a DynaCool Physical Properties Measurement System (Quantum Design) to derive the volume-integrated magnetic hysteresis loops and temperature dependence of the saturation magnetization $M_s(T)$. The blocking temperatures of the nanogranular films were extracted from the noise-filtered $M_s(T)$ curves using a Savitzky–Golay filter with a 12.5 K window and second-order polynomial. The angular dependence of the magnetization reversal was determined by means of magneto-optical magnetometry with a spatial resolution <0.5 mm and long-term stability guaranteed by dual-phase lock-in amplification of probe (1.4 kHz) and reference (1.68 kHz) beam [65]. Longitudinal and transverse magnetization components were simultaneously visualized on the micrometer scale using a full-field magneto-optical Kerr effect microscope (Evico Magnetics GmbH) with a magnification of 50 × (resolution: 235 nm) and modulated LED illumination. The transverse resistivity, reflecting the anomalous Hall effect, was obtained in van-der-Pauw geometry using the electrical transport option (177 Hz) of the DynaCool system.

Broadband spectroscopy of FMR leveraged a CryoFMR (NanOsc Instruments) inside the DynaCool system. The samples were placed face-down on a coplanar waveguide that probes an area of roughly 0.65 mm^2 along its 250 μm-wide conductor. To enhance sensitivity, the field derivative of the absorption intensity was detected using a constant-frequency excitation field via two Helmholtz coils and sweeping the DC magnetic bias field across the resonances. A Savitzky–Golay filter with window length 19, equivalent to $(3-8)$ kAm^{-1}, and a second-order polynomial was applied to the resulting spectra to reduce noise while maintaining the width of the resonances.

The spin and orbital moments as well as the element-specific hysteresis loops were obtained from XMCD spectroscopy at beamline 4.0.2 at the Advanced Light Source (LBNL, Berkeley, CA) providing a degree of polarization of 0.9 and a circular polarization across the entire energy range. The x-ray absorption spectra (XAS) near the Fe $L_{3,2}$ $[(690-750)$ eV] and the Ge $L_{3,2}$ $[(1200-1290)$ eV] edges were recorded using total electron yield (surface, probing depth of about 6 nm) and luminescence electron yield (bulk) while applying an external magnetic field (± 318 kA m^{-1}). The luminescence yield signal was obtained by illuminating a luminescent Al_2O_3 substrate downstream with the transmitted x-rays.

Imaging of the magnetization configuration on the sub-micrometer scale and at cryogenic temperatures was achieved by operating TEAM I in Lorentz mode. The films were allowed to thermally equilibrate for 30 min at each set temperature before the image sequences (1002 frames within 8 s) were recorded. The objective lens served as a solenoid to create a magnetic field along the sample surface normal while monitoring the in-plane magnetization configuration. Images were recorded at a constant defocus value of -0.2 mm set by the Lorentz lens current to limit electrostatic contributions.

Thermal spin fluctuations in the absence of an external magnetic field were investigated using coherent soft x-ray scattering and XPCS at beamline 23-ID-1 at the National

Synchrotron Light Source II (BNL, Upton, NY). After the set cryogenic temperature was reached and stable, the system was allowed to thermally equilibrate for 30 min before starting to record the time series. Element specificity to the out-of-plane magnetization component was provided by illuminating the sample at normal incidence and tuning the energy of circularly polarized photons to the Fe L_3 edge. The high coherent flux enabled us to probe the spin dynamics with a 10 Hz temporal resolution.

3. Results and discussion

3.1. Nanogranularity

The iron germanium films possess a nanogranular texture (figure 1(a), supporting figure 2) with a root mean square roughness of 5 nm that mainly depends on the grain size distribution (table 1). Calculating the Fourier transforms of the topography (figure 1(b), supporting figure 2) divulges an isotropic distribution of short-range-ordered grains with an average grain size of 55 nm that varies with film thickness and effective growth temperature (table 1). The grains deviate from an isotropic shape and are physically connected (figures 1(b) and (c)) and, as evident from magnetic imaging (figure 5), exchange coupled. A spatially varying grain contrast in transmission electron microscopy (figure 1(c)) suggests different crystallographic orientations in each grain. This nanocrystallinity is also apparent in the electron diffraction that unveils individual reflexes and two sharp faint rings as well as a prominent broad ring characteristic of an amorphous structure (figure 1(c)).

The formation of nanocrystals within an amorphous iron germanium structure is corroborated by x-ray diffraction. Figure 1(d) plots the two-theta scans for the bare substrate and iron germanium films S1 and S2 (table 1), revealing prominent silicon and FeGe reflexes at large and small angles, respectively. The bottom graph displays the two-theta scans for the substrate and nanogranular iron germanium films S3 and S5 (table 1) without apparent crystallinity, i.e. exhibiting an amorphous nanogranular structure. Amorphous silicon nitride appears as a broad peak around 33°. In addition, we observe two pronounced reflexes at 33.1° and 38.28° that are identified as (111) and (200) of cubic B20 FeGe according to the Bragg condition $2\theta = 2\arcsin[\lambda/(2d_{hkl})]$ with $\lambda = 0.154$ nm (Cu-K_α) and $d_{khl} = a/\sqrt{h^2+k^2+l^2}$. The extracted out-of-plane lattice constant a for FeGe(111) is similar to $a = 0.4679$ nm for epitaxial B20 FeGe(111) on Si(111) [66–68] while FeGe(200) requires a larger value of $a = 0.469$ nm. Except for a less significant peak at 44.5° that may originate from cubic Fe(110) at 44.76° or hexagonal B35 FeGe(002) at 44°, no indications of antiferromagnetic iron germanium, such as B35 FeGe [69, 70] and monoclinic FeGe [71], or Ge nanocrystals [70] were found. The overall small intensity of B20 FeGe reflexes agrees with earlier works on amorphous iron germanium films with similar composition that were assigned to exhibit a short-range order resembling that of B20 FeGe [36, 72].

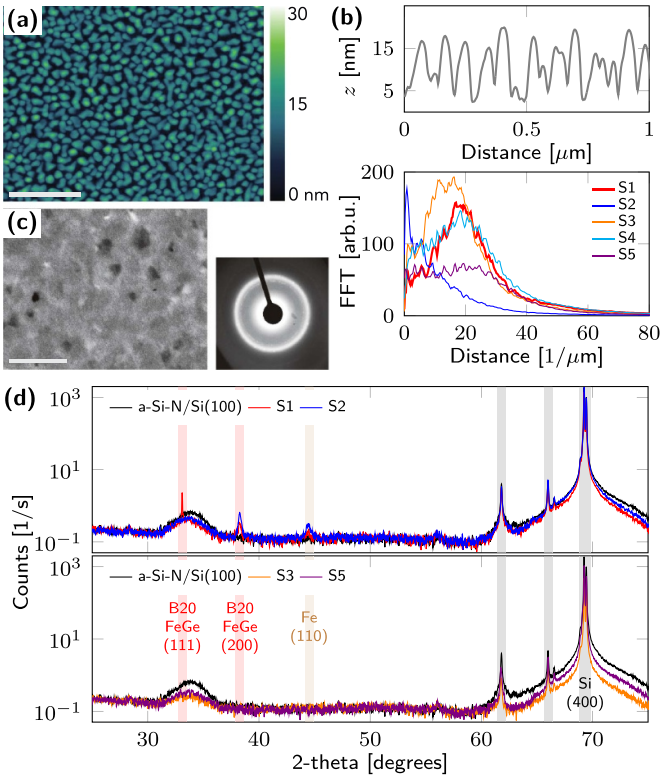

Figure 1. Structural properties of nanogranular iron germanium films on silicon nitride substrates and membranes characterized using (a), (b) atomic force microscopy, (c) transmission electron microscopy, and (d) x-ray diffraction. Scale bar is (a) 500 nm and (c) 100 nm. (b) Line profile and angle-averaged Fourier transform to determine the grain size. (c) Selected-area electron diffraction using a 10 μm pinhole revealing an isotropic distribution of nanocrystalline grains. Microscopy data are shown for S1. (d) Two-theta x-ray diffraction scans confirming growth of (top) B20 FeGe nanocrystals within an amorphous structure and (bottom) pure amorphous structure.

Moreover, observing nanogranular amorphous structures with and without embedded nanocrystals, governing the coordination and magnetic properties, is consistent with full-field transmission electron microscopy. The latter unveiled nanocrystals smaller than their respective grains (figure 1(c)) owing to the existence of a disordered shell likely associated with segregation.

3.2. Magnetization switching

The substrate growth temperature, coordination [73], surface roughness, and granularity have a profound impact on the temperature dependence of the saturation magnetization M_s (figure 2(a)). Despite having virtually the same net composition (table 1), each sample behaves differently showcasing the high sensitivity of magnetic properties to the local atomic environment and the need for a holistic study. This work focuses on 30 nm-thick nanogranular films with B20 FeGe nanocrystallites (S1) that defy both Bloch law [74] and

empirical expression $M_s(T) = M_s(0\ \mathrm{K})\left[1-\left(\frac{T}{T_c}\right)^{\eta}\right]^{\delta}$ [65], which is typically used to differentiate 3D Ising models ($\delta = 0.375$) [75, 76] and 2D Ising models ($\delta = 0.125$) [77] as well as homogeneous films ($\eta = 1.5$) [36, 74] and nanogranular films ($\eta \gtrsim 2$) [78, 79]. Among the displayed $M_s(T)$ curves, S1 is unique in the sense that the saturation magnetization linearly increases with decreasing temperature, likely due to the coexistence of ferromagnetic and paramagnetic phases above the blocking temperature T_B, which is found to depend on grain size rather than crystallinity (table 1). DC and AC magnetic susceptibility peak around $T_B = 24$ K and 35 K, respectively (figure 2(b)), indicating a phase transition that appears more prominent and at higher temperature in the 60 nm-thick films with larger grains and surface roughness (figure 2(a)). The blocking temperature agrees well with earlier works on epitaxial polycrystalline B20 FeGe on Ge(100) [80] but does not infer a complete transition between ferromagnetism and superparamagnetism as demonstrated by magnetometry (figures 2(c)–(e)) and magnetic imaging (figure 5). In comparison with epitaxial B20 FeGe(111), the saturation magnetization of S1 on a rigid substrate is roughly 70%, i.e. 225 kA m^{-1} (0.65 μ_B per iron atom) vs. 330 kA m^{-1} (0.924 μ_B per iron atom) [67, 81].

All nanogranular films are soft-magnetic with a preferred in-plane magnetization and are nearly isotropic in the plane (figures 2(c)–(e)). The transverse resistivity is plotted in arbitrary units to retrieve the saturation field by extrapolation and to quantify the magnetic anisotropy for S1 according to $K_u = \frac{1}{2}\mu_0 H_s M_s$ as $K_u(300\ \mathrm{K}) = (11 \pm 3)$ kJ m^{-3} and $K_u(100\ \mathrm{K}) = (52 \pm 6)$ kJ m^{-3}. Subtracting contributions from the demagnetization field yields the intrinsic magnetic anisotropy $K_{ui} = K_u - \frac{1}{2}\mu_0 M_s^2 N$ with the demagnetization factor N. The small saturation magnetization reduces the impact of the demagnetization factor that takes unity for an infinite plane geometry but can become $N \gtrsim 0.5$ for nanogranular films [82]. A rough estimate of $N = 0.9$ infers a change in K_{ui} that is within the experimental uncertainty. The demagnetization factor can further decrease if the intergranular exchange weakens as observed in films on membranes (figure 5). The corresponding in-plane magnetic anisotropy increases with decreasing temperature $K_{ui}(300\ \mathrm{K}) = (8.3 \pm 3)$ kJ m^{-3} and $K_{ui}(100\ \mathrm{K}) = (32.2 \pm 7)$ kJ m^{-3} suggesting a significant strengthening of magnetic exchange with decreasing temperature in agreement with the temperature dependence of the saturation magnetization derived from FMR spectroscopy (figure 3(f)).

Films on silicon nitride substrates with a remanent in-plane magnetization of $(0.25-0.5)\ M_s$ exhibit a room-temperature coercive field ranging from 0.4 to 0.5 kA m^{-1} that decreases, due to strain relaxation, on the membrane within a few tens of micrometers from the frame (rigid support) to $(0.15-0.3)$ kA m^{-1}. Regions further away from the substrate do not reveal any magnetic signal detectable by magneto-optical means. This observation is consistent with low-temperature iron germanium films that possess a large uniaxial strain and larger saturation magnetization compared with room-temperature films (supporting figure 3). Markedly, a magnetic hysteresis loop with a coercive field of 1 kA m^{-1}

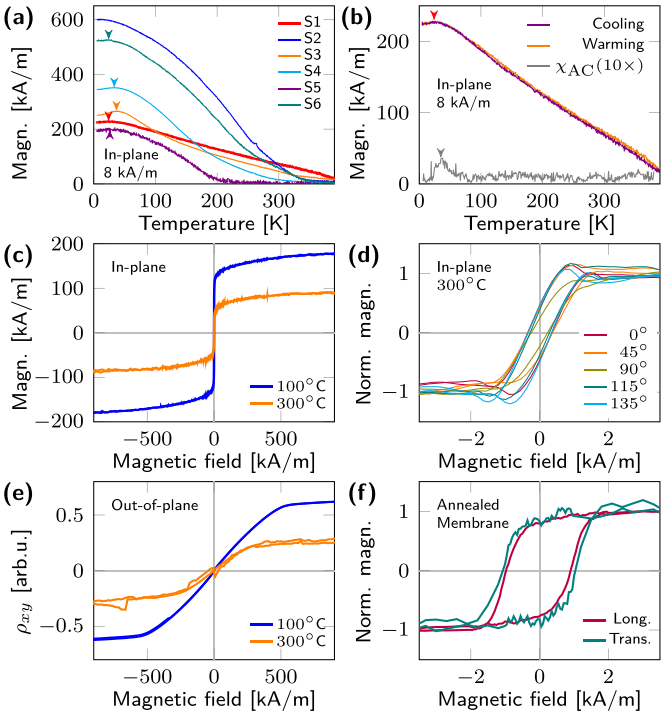

Figure 2. Magnetization switching in nanogranular iron germanium films on silicon nitride substrates. (a) Temperature dependence of saturation magnetization for various nanogranular films retrieved from vibrating sample magnetometry. (b) Saturation magnetization for S1 and AC susceptibility. Arrows in (a) and (b) indicate blocking temperatures. (c), (d) In-plane magnetic hysteresis loops for S1 recorded with (c) vibrating sample magnetometry and (d) magneto-optical Kerr effect magnetometry corroborating nearly isotropic magnetic properties. (e) Transverse resistivity for S1 obtained in van-der-Pauw geometry. (f) Room-temperature hysteresis loops for longitudinal and transverse magnetization components in annealed films (S1) on flexible membranes measured simultaneously with Kerr microscopy (field applied in longitudinal direction).

and remanent magnetization of 0.8 M_s emerges after thermal annealing (figure 2(f)) due to sustained resonant x-ray illumination that alters the coordination without affecting the composition. This tendency is in agreement with an increased saturation magnetization following annealing of iron germanium [73] and laser-induced ordering generating ferromagnetism [43].

3.3. Ferromagnetic resonances

The locally varying orientation of the magnetic anisotropy and saturation magnetization in the nanogranular films is apparent in multiple nearby FMR and a sizable inhomogeneous line broadening. The spectra taken for S1 in out-of-plane geometry, i.e. DC magnetic bias field applied along the surface normal and in-plane AC driving field, reveal numerous prominent resonances (figure 3(a)) due to slightly different grain orientation concurrent with transmission electron microscopy (figure 1(c)). Two-magnon scattering [83–85] on defects and nanogranular boundaries [86] in in-plane geometry causes spin dephasing, less pronounced individual

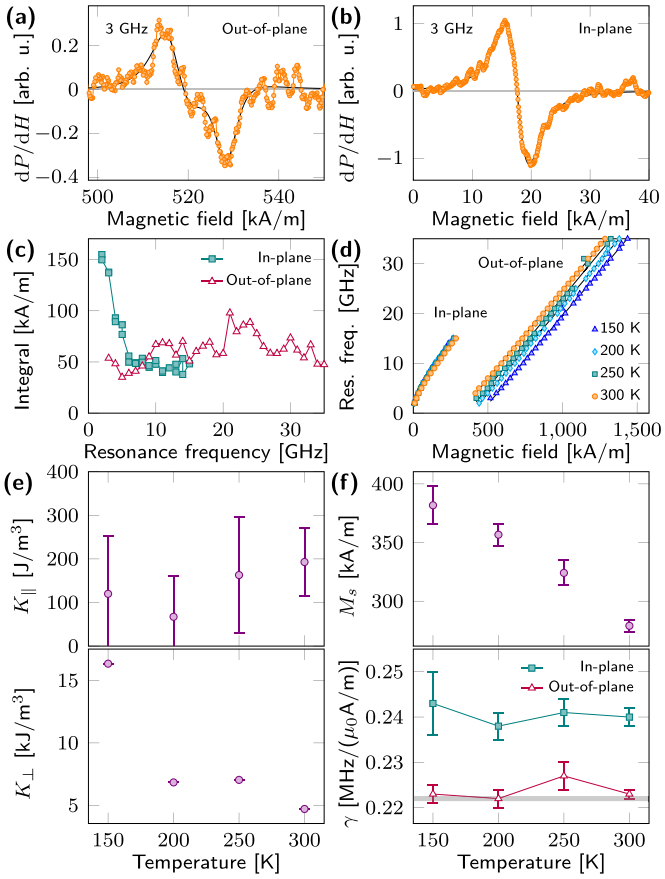

Figure 3. Ferromagnetic resonances in S1 films on silicon nitride substrates. (a) Out-of-plane and (b) in-plane ferromagnetic resonance spectra taken at 150 K consisting of multiple nearby resonances. The in-plane and out-of-plane resonance is fitted using one and two derivatives of the sum of symmetric and asymmetric Lorentzians, respectively. (c) Integrated power absorption derivative. (d) Dependence of the ferromagnetic resonance on magnetic bias field. (e) In-plane and out-of-plane magnetic anisotropy corroborating lateral isotropic strain and a preferential in-plane easy-plane spin orientation. (f) Saturation magnetization substantially larger than the magnetometry value and temperature-independent anisotropic gyromagnetic ratio γ. Horizontal line indicates free-electron value ($m_o = 0$).

resonances (figure 3(b)), an overall broader resonance, and a rapid decline of the absorption intensity with increasing excitation frequency (figure 3(c)). The in-plane and out-of-plane spectra are fitted using one (single-peak) and two (double-peak) derivatives of the sum of symmetric and asymmetric Lorentzians [87], respectively. While increasing the number of fitted resonances (double-peak, triple-peak etc) generally yields better fits, an exceedingly large number of fitting parameters makes the analysis arbitrary and does not significantly change the extracted physical quantities except for the inhomogeneous line broadening. The calculated quality factor for out-of-plane geometry ranges from 50 to 100 for double-peak fitting and from 25 to 30 for single-peak fitting. This is in stark contrast to the in-plane quality factor of 2–5 (single-peak-fitting). Note that this collective value underestimates the quality factor for individual grains.

Fitting the analytical expressions for the relationship between resonance frequency and resonance field [87–89]:

$$2\pi f_{\text{res}}^{\parallel} = \gamma\mu_0 \sqrt{\left(H_{\text{res}}^{\parallel} + H_{\parallel}\right)\left(H_{\text{res}}^{\parallel} + H_{\parallel} - H_{\perp} + M_s\right)},$$
$$2\pi f_{\text{res}}^{\perp} = \gamma\mu_0 \left(H_{\text{res}}^{\perp} - H_{\perp} - M_s\right),$$

to the experimental in-plane and out-of-plane data, respectively, (figure 3(d)) allows for quantifying the in-plane ($H_\parallel$) and perpendicular ($H_\perp$) magnetic anisotropy fields related to the respective anisotropies via $K = \frac{1}{2}\mu_0 M_s H$ (figure 3(e)) as well as the saturation magnetization M_s and the gyromagnetic ratio γ (figure 3(f)). The negligible in-plane anisotropy despite strong spin damping is consistent with magnon scattering at grain boundaries and the isotropic behavior of the angle-dependent magnetometry data (figure 2(d)). Both sign and magnitude of the easy-plane magnetic anisotropy $K_\perp$ are concurrent with magnetic hysteresis loops (figures 2(c)–(e)) suggesting a strengthening of magnetic exchange with decreasing temperature. In addition, FMR spectroscopy reveals a substantially larger saturation magnetization compared with vibrating sample magnetometry (figures 2(a) and 3(f)), indicating the aforementioned segregation at, e.g. grain boundaries and/or contributions from Fe(110) nanocrystals.

3.4. Anisotropic orbital hybridization

The gyromagnetic ratios derived from FMR spectroscopy are persistently different for in-plane and out-of-plane geometry and nearly independent of both temperature and number of resonances used for fitting (figure 3(f)). This discrepancy is inherent to the nanogranular iron germanium films and not a measurement artifact as prior studies using, e.g. single-crystal yttrium iron garnet revealed nearly perfect agreement between vibrating sample magnetometry and FMR spectroscopy values and an orientation-independent Landé factor g [87]. The gyromagnetic ratio $\gamma = g\frac{\mu_B}{\hbar} = g\frac{e}{2m_e}$ is directly proportional to the ratio of orbital (m_o) to spin (m_s) moment [90]:

$$\frac{m_o}{m_s} = \frac{g-2}{2} = \gamma\frac{m_e}{e} - 1,$$

and provides insight into the anisotropic orbital hybridization in terms of the averaged local atomic environment. Here, we use the Bohr magneton μ_B, the free electron mass m_e, and the elementary charge e. For out-of-plane geometry, we obtain $\gamma = 0.222$ MHz $(\mu_0 \text{A m}^{-1})^{-1}$ corresponding to $g = 2.009$ and $\frac{m_o}{m_s} = 0.004$ that are close to values for free electrons. The in-plane values are significantly larger, namely, $\gamma = 0.24$ MHz $(\mu_0 \text{A m}^{-1})^{-1}$, $g = 2.17$, and $\frac{m_o}{m_s} = 0.086$. Note that neither calculation considered contributions from germanium or spin mixing that is reportedly negligible in iron compounds compared with, e.g. nickel and cobalt [91]. Comparing these quantities with literature values for pure iron

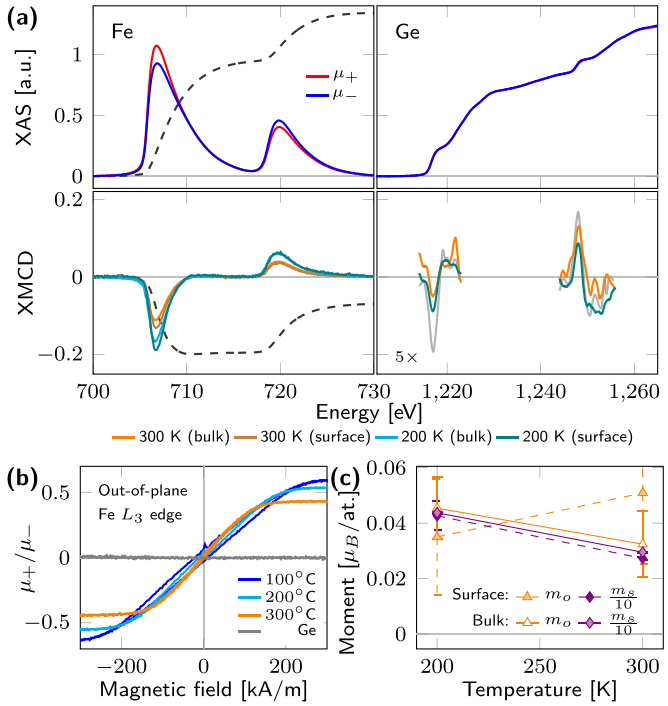

Figure 4. X-ray absorption spectroscopy and iron moment derived from x-ray magnetic circular dichroism in S1 films on silicon nitride membranes. (a) Absorption and dichroism spectra near Fe and Ge L_3 edges for bulk and surface regions. Gray Ge dichroism spectrum is recorded with iron-rich sample. (b) Element-specific out-of-plane magnetic hysteresis loops revealing saturation fields for membranes $H_{\text{sat}}^{\text{mem}} \approx \frac{1}{2} H_{\text{sat}}^{\text{sub}}$ smaller than for substrates. (c) Spin and orbital moments for iron using iron electron hole density.

($g = 2.085$, $\frac{m_o}{m_s} = 0.042$) [91, 92] suggests a deformation of the Fe 3d orbitals by germanium or the lateral isotropic strain and/or an orientation-dependent spin mixing.

The corresponding hybridization between Fe *d* levels and Ge *sp* band states is evident from XAS/XMCD spectroscopy in terms of an induced germanium moment (figure 4(a)) that increases with the iron concentration and is parallel to the iron moment. Correlating the element-specific out-of-plane magnetic hysteresis loops for iron with the transverse resistivity (figure 2(e)) reveals a saturation field that is 50% smaller for films on membranes than on substrates owing to strain relaxation (figure 4(b)). Switching of the germanium moment could not be resolved. Further comparison is given in terms of the iron orbital-to-spin moment ratio, quantified using the sum rules $\frac{m_o}{m_s} = \frac{4}{3}\frac{q}{6p-4q}$ [93, 94] with the spectrum integrals $q = \int_{L_3+L_2} (\mu_+ - \mu_-)\,\mathrm{d}\omega$ and $p = \int_{L_3} (\mu_+ - \mu_-)\,\mathrm{d}\omega$. The experimental uncertainty is dominated by statistical errors of consecutive spectra and the omission of the dipole operator term [95]. Within experimental uncertainty, the orbital-to-spin moment ratio is 0.1 and independent of temperature and region, i.e. surface or bulk, (figure 4(c)) and consistent with earlier work on amorphous iron germanium films with similar composition [36]. This infers that both surface and bulk regions have similar properties in contrast to Co–Si nanocrystals that developed a non-magnetic core and ferromagnetic shell [96]. An orbital-to-spin moment ratio of 0.1 corresponds to $g = 2.222$ and differs markedly from the FMR data (figure 3(f)). It is important to note that the FMR spectroscopy values are obtained with nanogranular films on substrates while XMCD spectroscopy uses relaxed nanogranular films on membranes. In addition, FMR values can be substantially smaller than XMCD data owing to contributions from the dipole operator, effectively decreasing the spin moment at the surface by $< 10\%$ in XMCD [95], and the neglect of a possible spin mixing that could notably increase the orbital-to-spin moment ratio in FMR spectroscopy [91]. Moreover, the spin and orbital moments, calculated using the charge carrier concentration of pure iron, are mere estimates since the carrier concentration strongly depends on composition and short-range order. The moments are one order of magnitude smaller than for iron [97] and considerably smaller than $M_s(0\ \text{K}) \approx 1\ \mu_B$ per Fe atom observed in B20 FeGe single-crystals [67, 81] and amorphous films [36].

3.5. Magnetization configuration in strained and relaxed films

Confirmation of the anisotropy and inhomogeneity of magnetic properties, deduced from spectroscopy and magnetometry, is given by visualizing the in-plane magnetization components with Kerr and Lorentz microscopy. The former confirms a soft-magnetic film on the rigid substrate with a sizable in-plane magnetization at room temperature. A branching-like domain pattern [98] develops in the transition region between frame and membrane due to locally varying strain that weakens the magnetic anisotropy, exchange, and saturation magnetization (figure 5(a)). The domain walls branch out perpendicular to the edge along the strain gradient and are particularly prominent after AC demagnetization. The reduction in magnetic anisotropy and exchange causes the room-temperature saturation magnetization to virtually vanish within 50 μm from the frame. A phase transition from the nearly non-magnetic to a ferromagnetic system with macroscopic domains (figure 5(b), also figure 2(f)) can be triggered by local thermal annealing, inducing an optically visible change in topography. To this end, sustained illumination with resonant x-rays provides a means to alter the coordination of the nanogranular film, similar to laser-induced ordering [43], while preserving its macroscopic composition.

The weak magnetic contrast in S1 films on membranes is spatially resolved with Lorentz microscopy using the transport-of-intensity equation [99]. Assuming a spatial confinement of the magnetic induction to the nanogranular film and a magnetic induction solely due to the magnetization, i.e. neglecting any magnetic stray field contributions, allows for deriving the in-plane components of the magnetization as the two-dimensional gradient of the reconstructed electron phase [100]. The complete set of electron intensities, reconstructed electron phases, and magnetization configurations is shown in supporting figures 4–6. To verify the magnetic origin of the contrast and negligible pinning at defects/grains, the sample was exposed to a magnetic field (4.8 kA m^{-1}) applied along the surface normal inducing a noticeable change in the

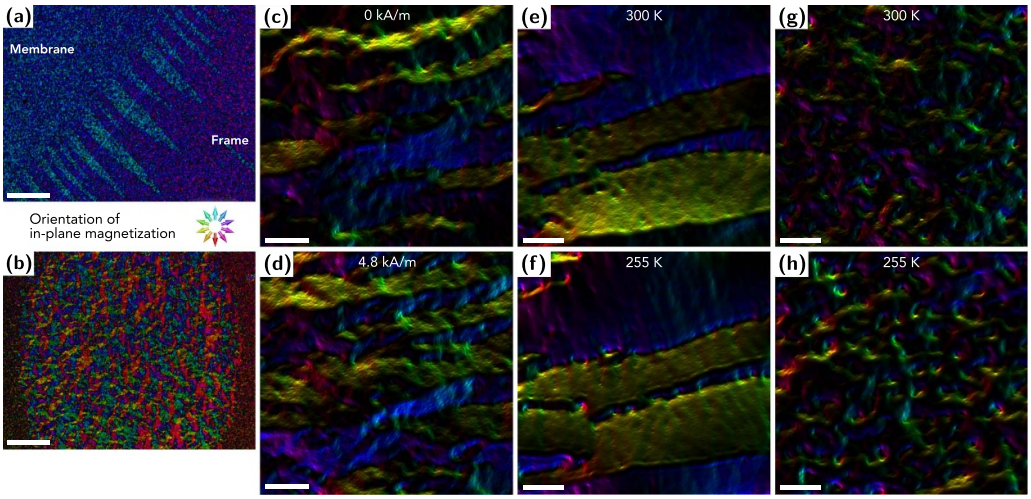

Figure 5. Magnetization configuration in S1 films on silicon nitride membranes visualized with Kerr and Lorentz microscopy. (a) Branching-like domain pattern forming as AC demagnetized room-temperature configuration near transition between flexible membrane and rigid substrate. (b) Magnetic contrast on membrane appearing after local thermal annealing at room temperature. (c), (d) Room-temperature in-plane magnetic induction of the same area near the frame at (c) remanence and (d) in the presence of an out-of-plane magnetic field (4.8 kA m^{-1}) confirming intergranular exchange and formation of non-collinear spin textures in ferromagnetic phase. In-plane magnetic induction (e), (f) near the frame and (g), (h) near the central region of the membrane. The 255 K phases unveil an increased density and intensity of magnetic contrast originating from non-collinear spin textures. The striped contrast perpendicular to the main magnetization component in (e), (f) strengthens with decreasing temperature. In-plane components of magnetization are represented by color shown as inset in (a). Scale bar is (a), (b) 30 μm and (c)–(h) 300 nm.

in-plane magnetization. This is demonstrated for a region near the frame with ferromagnetic domains (figures 5(c) and (d), supporting figure 4). A closer look reveals tolerable electrostatic contributions despite nanogranularity and nanocrystallinity that do not disturb the magnetic contributions.

The magnetization near the frame does not fundamentally change by cooling the sample down to 255 K (figures 5(e) and (f)), yet unveils crucial details. Ferromagnetic domain walls are mobile and domains can break up. The presumed structural contributions at room temperature (left side of figure 5(e)) vanish indicating a pure magnetic origin. A similar rationale applies to the decoration of domain walls with chiral spin textures at cryogenic temperatures that suggests the possibility to find them also in films on silicon nitride substrates in spite of a stronger ferromagnetic coupling. The striped contrast perpendicular to the main magnetization component strengthens and straightens with decreasing temperature. Its regular periodicity, orientation, and long-range order hint at the formation of meander domains as a precursor phase to helical or conical spin lattices [36]. In contrast, the weakening of magnetic anisotropy, exchange, and saturation magnetization near the central region of the membrane causes a disordered skyrmion phase with a feature size $\lesssim 100$ nm (figures 5(g) and (h)) similar to those observed in amorphous iron germanium films [36]. Note that the field of view might slightly differ due to the lack of resemblance (fiducial markers for alignment). The 255 K phases exhibit an increased density and intensity of magnetic contrast originating from the chiral spin textures while electrostatic contributions remain unchanged. The formation of a topological state on the surface of nanogranular structures, due to curvature-induced Dzyaloshinskii–Moriya-like interaction [101, 102], is unlikely because of existing intergranular exchange and similar spin and orbital moments for surface and bulk regions (figure 4(c)). The surface and bulk regions should differ to guarantee a magnetic shell instead of a solid magnetic geometry [96].

By analogy with the magnetic field manipulation (figures 5(c) and (d)), neither spin configuration reveals noticeable pinning at defects or confinement to individual granular regions. Given the structural properties of the 30 nm-thick nanogranular films with B20 FeGe nanocrystal inclusions, S1 could function as a disordered two-dimensional magnetic shift register or be used for reservoir computing [21, 103] owing to thickness modulation and variations in crystallinity and crystal orientation.

3.6. *Interaction between topological magnetic states*

A quantitative estimate of the coupling between the topological states is given in terms of speckle analysis [104] with XPCS associated with the ordering of the out-of-plane magnetization component of the skyrmion cores at remanence. The Fraunhofer diffraction of the coherent resonant x-ray beam deflecting from the sample lacks a well-defined symmetry (ring instead of Bragg peaks) (figure 6(a)) due to the absence of long-range-ordered helical or skyrmion phases, observed in other amorphous materials [37, 105, 106], which is consistent with the microscopy data (figures 5(g) and (h)). A representative waterfall plot (temporal evolution of a line profile) through the speckle pattern, showcasing its dynamics, is displayed in figure 6(b). The complete set of diffraction patterns and a selection of waterfall plots are shown in

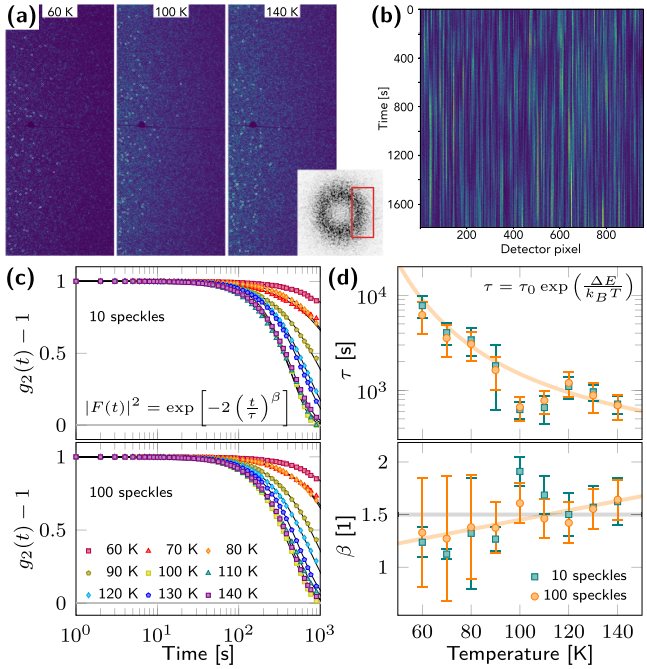

Figure 6. Thermal spin fluctuations in S1 films on silicon nitride membranes probed with resonant coherent x-ray scattering at remanence and the Fe L_3 absorption edge using circularly polarized photons. (a) Speckle pattern with the 100 most intense reflexes highlighted, which were used for x-ray photon correlation spectroscopy. The large isotropic ring pattern exceeds the detector area leading to a partially covered reciprocal space as illustrated by the inset. (b) Representative waterfall plot of speckle pattern revealing spin dynamics at 100 K. (c) Normalized autocorrelation functions $g_2 - 1$ for the ten and 100 most prominent speckles with fit to extract relaxation time τ and critical exponent β shown in (d). Fits for the critical exponent assume a linear dependence on the temperature and a temperature-independent value, respectively.

supporting figures 7 and 8. The normalized autocorrelation functions $g_2 - 1$ for the ten and hundred most intense speckles, highlighted in figure 6(a), are individually computed (supporting figures 9 and 10) and averaged (figure 6(c)) to obtain the intermediate scattering function, i.e. dynamical structure factor $F(\mathbf{q},t)$ assuming a beam coherence $A = 1$ according to [107, 108]:

$$g_2(\mathbf{q},t) - 1 = \frac{\langle I(\mathbf{q},\tau) I(\mathbf{q},\tau+t)\rangle_\tau}{\langle I(\mathbf{q},\tau)\rangle_\tau^2} - 1 = A|F(\mathbf{q},t)|^2 .$$

The resulting correlation functions are fitted with the analytical expression:

$$|F(\mathbf{q},t)| = \exp\left[-\left(\frac{t}{\tau}\right)^{\beta}\right] ,$$

to extract relaxation time τ and critical exponent β (figure 6(d)) that provide information about the characteristics of the interaction, i.e. liquid-like (spin glass) vs. solid-like (collective). The experimental uncertainty originates from the standard deviation of individual $g_2 - 1$ functions that is 100 times larger than the error from fitting the averaged $g_2 - 1$ function (figure 6(c)). Both relaxation time and critical exponent are fairly independent of the chosen speckle, i.e. reciprocal lattice vector (periodicity and orientation) (supporting figures 9 and 10), and are, except for near 100 K, well described by exponential and linear fits, respectively (figure 6(d)). The physical origin of this anomaly is unclear. The temperature dependence of the relaxation time is described with two different theories that yield similar activation energy barriers ΔE for the probed temperature range:

$$\tau = \tau_0 \exp\left(\frac{\Delta E}{k_B (T - T_0)}\right) .$$

Non-interacting particles whose magnetization reversal involves a single relaxation pathway and activation barrier can be described by the Arrhenius-type Néel–Brown theory [109, 110] with $T_0 = 0$ K that yields $\Delta E = 23$ meV and an activation temperature $\Delta E/k_B \approx 270$ K above which skyrmions disappear. The Vogel–Fulcher–Tammann theory [111–113], accounting for magnetic coupling between particles, typically used to model spin glasses with disordered exchange coupling (liquid-like), gives $\Delta E = 17$ meV and a freezing temperature $T_0 \approx 10$ K below which spin fluctuations of the skyrmions are suppressed. The latter coincides with the blocking temperature $T_B = (24 \sim 35)$ K for S1 films retrieved from AC and DC susceptibility measurements (figure 2(b)). However, spin glass dynamics are shown to exhibit $\beta < 1$ that is only reached at absolute temperature assuming a linear dependence (figure 6(d)). The derived activation temperature agrees reasonably well with the microscopy data (figure 5) that reveal the fading of magnetic contrast and topological states at room temperature.

4. Conclusion

The synthesis of Fe_xGe_{1-x} films ($x = 0.53 \pm 0.05$) revealed a germanium adhesion $\gtrsim 50\%$ and a nanogranularity that dominated the temperature dependence of the saturation magnetization, including its absolute value and the coexistence of ferromagnetic and paramagnetic phases above the blocking temperature $T_B \approx 30$ K. Nanogranular films (30 nm-thick) with B20 FeGe nanocrystals embedded in an amorphous structure exhibited a saturation magnetization that linearly increases with decreasing temperature from 70 kA m^{-1} (300 K) to 225 kA m^{-1} (0 K). The magnetic anisotropy values derived from magnetometry and FMR spectroscopy coincided with each other in stark contrast to the saturation magnetization hinting at a phase segregation at, e.g. the amorphous grain boundaries. The out-of-plane orbital moment nearly vanished while the in-plane Landé factor was significantly larger ($g = 2.17$) than the literature value for pure iron ($g = 2.085$) [91, 92] suggesting a deformation of the Fe 3d

orbitals by Ge as evident from an induced germanium moment and due to the lateral isotropic strain. The transition from a soft-magnetic ferromagnetic phase on a rigid substrate to a disordered skyrmion phase with a feature size $\lesssim$100 nm and without a helical precursor phase in relaxed films on membranes was mediated by the formation of branching-like domain patterns. Neither spin configuration revealed noticeable pinning at defects or confinement to individual granular regions. The activation temperature of the weakly coupled topological states (270 K) derived from XPCS agreed well with the microscopy data that revealed the fading of magnetic contrast and topological states at room temperature.

Our results demonstrate that rigid wafers and free-standing membranes yield distinct physical properties due to varying deposition conditions (thermal conductance) and strain relaxation, generally preventing the inference from one batch to another. The observed strain manipulation of magnetic exchange and topological magnetism is expected to be more prominent in amorphous structures lacking nanogranularity and nanocrystallinity and may benefit, in combination with piezoelectric substrates, physical reservoir computing with topological spin textures. A quantification of the strain control will require a thorough investigation of its composition and coordination dependence and the determination of magnetostriction constants.

Data availability statement

All data that support the findings of this study are included within the article (and any supplementary files).

Acknowledgments

This work was primarily supported by the National Science Foundation, Division of Materials Research under Grant No. 2203933. R S and O T acknowledge support by the National Science Foundation/EPSCoR RII Track-1: Emergent Quantum Materials and Technologies (EQUATE) under Grant No. OIA-2044049. Work at the Molecular Foundry was supported by the U.S. Department of Energy, Office of Science, Basic Energy Sciences under Contract No. DE-AC02-05-CH11231. This research used resources of the Advanced Light Source, which is a DOE Office of Science User Facility under Contract No. DE-AC02-05-CH11231. This research used resources at beamline CSX, 23-ID-1 of the National Synchrotron Light Source II, a U.S. Department of Energy (DOE) Office of Science User Facility operated for the DOE Office of Science by Brookhaven National Laboratory under Contract No. DE-SC0012704. Resources were made available through BNL/LDRD#19-013. The research was performed in part in the Nebraska Nanoscale Facility: National Nanotechnology Coordinated Infrastructure and the Nebraska Center for Materials and Nanoscience, which are supported by the National Science Foundation under Award ECCS: 2025298, and the Nebraska Research Initiative.

ORCID iDs

Ruthi Zielinski https://orcid.org/0000-0003-3719-0699
Nhat Nguyen https://orcid.org/0000-0002-1095-1585
Bryce Herrington https://orcid.org/0000-0002-1481-0464
Omar Taha https://orcid.org/0009-0008-6274-0596
Wai Kiat Chin https://orcid.org/0000-0002-1840-0825
Ather Mahmood https://orcid.org/0000-0001-7170-1646
Padraic Shafer https://orcid.org/0000-0001-9363-2557
Jim Ciston https://orcid.org/0000-0002-8774-5747
Paul Ashby https://orcid.org/0000-0003-4195-310X
Claudio Mazzoli https://orcid.org/0000-0001-9774-1507
Robert Streubel https://orcid.org/0000-0003-4783-892X

References

[1] Dzyaloshinskii I E 1957 *Sov. Phys.-JETP* **5** 1259
[2] Moriya T 1960 *Phys. Rev.* **120** 91–98
[3] Yu X Z, Onose Y, Kanazawa N, Park J H, Han J H, Matsui Y, Nagaosa N and Tokura Y 2010 *Nature* **465** 901
[4] Yu X Z, Kanazawa N, Onose Y, Kimoto K, Zhang W Z, Ishiwata S, Matsui Y and Tokura Y 2011 *Nat. Mater.* **10** 106
[5] Wilhelm H, Baenitz M, Schmidt M, Rößler U K, Leonov A A and Bogdanov A N 2011 *Phys. Rev. Lett.* **107** 127203
[6] Gayles J, Freimuth F, Schena T, Lani G, Mavropoulos P, Duine R A, Blügel S, Sinova J and Mokrousov Y 2015 *Phys. Rev. Lett.* **115** 036602
[7] Shibata K, Yu X Z, Hara T, Morikawa D, Kanazawa N, Kimoto K, Ishiwata S, Matsui Y and Tokura Y 2013 *Nat. Nanotechnol.* **8** 723
[8] Zheng F, Kiselev N S, Rybakov F N, Yang L, Shi W, Blügel S and Dunin-Borkowski R E 2023 *Nature* **623** 718
[9] Yu X, Liu Y, Iakoubovskii K V, Nakajima K, Kanazawa N, Nagaosa N and Tokura Y 2023 *Adv. Mater.* **35** 2210646
[10] Sutcliffe P 2017 *Phys. Rev. Lett.* **118** 247203
[11] Wang X S, Qaiumzadeh A and Brataas A 2019 *Phys. Rev. Lett.* **123** 147203
[12] Fert A, Cros V and Sampaio J 2013 *Nat. Nanotechnol.* **8** 152–6
[13] Sampaio J, Cros V, Rohart S, Thiaville A and Fert A 2013 *Nat. Nanotechnol.* **8** 839–44
[14] Parkin S and Yang S H 2015 *Nat. Nanotechnol.* **10** 195–8
[15] Schwarze T, Waizner J, Garst M, Bauer A, Stasinopoulos I, Berger H, Pfleiderer C and Grundler D 2015 *Nat. Mater.* **14** 478
[16] Seki S, Okamura Y, Shibata K, Takagi R, Khanh N D, Kagawa F, Arima T and Tokura Y 2017 *Phys. Rev.* B **96** 220404
[17] Chen S *et al* 2024 *Nature* **627** 522
[18] Urrestarazu Larrañaga J *et al* 2024 *Nano Lett.* **24** 3557
[19] Díaz S A, Klinovaja J and Loss D 2019 *Phys. Rev. Lett.* **122** 187203
[20] Díaz S A, Hirosawa T, Klinovaja J and Loss D 2020 *Phys. Rev. Res.* **2** 013231
[21] Raab K, Brems M A, Beneke G, Dohi T, Rothörl J, Kammerbauer F, Mentink J H and Kläui M 2022 *Nat. Commun.* **13** 6982
[22] Lee O *et al* 2024 *Nat. Mater.* **23** 79

[23] Schmitt M *et al* 2022 *Commun. Phys.* **5** 254
[24] Meisenheimer P *et al* 2023 *Nat. Commun.* **14** 3744
[25] Li Z *et al* 2024 *Nat. Commun.* **15** 1017
[26] Liu C, Zhang S, Hao H, Algaidi H, Ma Y and Zhang X X 2024 *Adv. Mater.* **36** 2311022
[27] Jin S *et al* 2024 *Nano Lett.* **24** 5467
[28] Huang Z, McCray A R C, Li Y, Morrow D J, Qian E K, Young Chung D, Kanatzidis M G, Phatak C and Ma X 2024 *Nano Lett.* **24** 1531
[29] Mitchell N P, Nash L M, Hexner D, Turner A M and Irvine W T M 2018 *Nat. Phys.* **14** 380
[30] Costa M, Schleder G R, Buongiorno Nardelli M, Lewenkopf C and Fazzio A 2019 *Nano Lett.* **19** 8941
[31] Corbae P *et al* 2023 *Nat. Mater.* **22** 200
[32] Pöyhönen K, Sahlberg I, Westström A and Ojanen T 2018 *Nat. Commun.* **9** 2103
[33] Yang Y B, Qin T, Deng D L, Duan L M and Xu Y 2019 *Phys. Rev. Lett.* **123** 076401
[34] Grushin A G and Repellin C 2023 *Phys. Rev. Lett.* **130** 186702
[35] Kim S, Agarwala A and Chowdhury D 2023 *Phys. Rev. Lett.* **130** 026202
[36] Streubel R *et al* 2021 *Adv. Mater.* **33** 2004830
[37] Singh A *et al* 2023 *Adv. Funct. Mater.* **33** 2300224
[38] Daver H and Massenet O 1977 *Solid State Commun.* **23** 393
[39] Randhawa H S, Malhotra L K, Sehgal H K and Chopra K L 1976 *Phys. Status Solidi* a **37** 313–20
[40] Liu X, Queen D R, Metcalf T H, Karel J E and Hellman F 2014 *Phys. Rev. Lett.* **113** 025503
[41] Temkin R, Paul W and Connell G 1973 *Adv. Phys.* **22** 581–641
[42] Gibson J M and Treacy M M J 1997 *Phys. Rev. Lett.* **78** 1074
[43] Pflug T *et al* 2024 *Adv. Funct. Mater.* **34** 2311951
[44] Coey J M D 1978 *J. Appl. Phys.* **49** 1646
[45] Bayaraa T and Griffin S M 2023 arXiv:2311.07725
[46] Sherrington D and Kirkpatrick S 1975 *Phys. Rev. Lett.* **35** 1792
[47] Edwards S and Anderson P 1976 *J. Phys. F: Met. Phys.* **6** 1927
[48] Weiler M, Dreher L, Heeg C, Huebl H, Gross R, Brandt M S and Goennenwein S T B 2011 *Phys. Rev. Lett.* **106** 117601
[49] Chen C, Han L, Liu P, Zhang Y, Liang S, Zhou Y, Zhu W, Fu S, Pan F and Song C 2023 *Adv. Mater.* **35** 2302454
[50] Gusev N S, Sadovnikov A V, Nikitov S A, Sapozhnikov M V and Udalov O G 2020 *Phys. Rev. Lett.* **124** 157202
[51] Nepal R, Güngördü U and Kovalev A A 2018 *Appl. Phys. Lett.* **112** 112404
[52] Yang W G and Schmidt H 2021 *Appl. Phys. Rev.* **8** 021304
[53] Chen R, Chen C, Han L, Liu P, Su R, Zhu W, Zhou Y, Pan F and Song C 2023 *Nat. Commun.* **14** 4427
[54] Miyazaki Y, Yokouchi T and Shiomi Y 2023 *Sci. Rep.* **13** 1922
[55] Yang Y *et al* 2024 *Nat. Commun.* **15** 1018
[56] Li S, Kang W, Huang Y, Zhang X, Zhou Y and Zhao W 2017 *Nanotechnology* **28** 31LT01
[57] Hu J M, Yang T and Chen L Q 2018 *npj Comput. Mater.* **4** 62
[58] Hu J M, Yang T and Chen L Q 2020 *Acta Mater.* **183** 145
[59] Mehmood N, Fazal R, Yadong W, Guo T, Zhang Q, Hou Z, Xingsen G and Liu J M 2021 *J. Magn. Magn. Mater.* **526** 167706
[60] Shi S, Zhao Y, Sun J, Yu G, Zhou H and Wang J 2024 *Nanoscale* **16** 12013–20
[61] Mathon O, Baudelet F, Itié J P, Polian A, d'Astuto M, Chervin J C and Pascarelli S 2004 *Phys. Rev. Lett.* **93** 255503
[62] Torchio R *et al* 2011 *Phys. Rev. Lett.* **107** 237202
[63] Pedrazzini P *et al* 2007 *Phys. Rev. Lett.* **98** 047204
[64] Sidorov V A, Petrova A E, Berdonosov P S, Dolgikh V A and Stishov S M 2014 *Phys. Rev.* B **89** 100403
[65] Adhikari A, Herrington B, Nguyen N, Zielinski R, Mahmood A, Adenwalla S and Streubel R 2023 *J. Phys.: Condens. Matter* **36** 015802
[66] Huang S X and Chien C L 2012 *Phys. Rev. Lett.* **108** 267201
[67] Porter N A, Gartside J C and Marrows C H 2014 *Phys. Rev.* B **90** 024403
[68] Ahmed A S, Esser B D, Rowland J, McComb D W and Kawakami R K 2017 *J. Cryst. Growth* **467** 38–46
[69] Forsyth J, Wilkinson C and Gardner P 1978 *J. Phys. F: Met. Phys.* **8** 2195
[70] Gallagher J C, Meng K Y, Brangham J T, Wang H L, Esser B D, McComb D W and Yang F Y 2017 *Phys. Rev. Lett.* **118** 027201
[71] Felcher G and Jorgensen J 1983 *J. Phys. C: Solid State Phys.* **16** 6281
[72] Bouma D S, Chen Z, Zhang B, Bruni F, Flatté M E, Ceballos A, Streubel R, Wang L W, Wu R Q and Hellman F 2020 *Phys. Rev.* B **101** 014402
[73] Kúkoľová A, Dimitrievska M, Litvinchuk A P, Ramanandan S P, Tappy N, Menon H, Borg M, Grundler D and Fontcuberta i Morral A 2021 *Cryst. Eng. Commun.* **23** 6506–17
[74] Bloch F 1930 *Z. Phys.* **61** 206
[75] Seeger M, Kaul S N, Kronmüller H and Reisser R 1995 *Phys. Rev.* B **51** 12585–94
[76] Pelissetto A and Vicari E 2002 *Phys. Rep.* **368** 549–727
[77] Zhang Z D 2007 *Phil. Mag.* **87** 5309–419
[78] Senz V, Röhlsberger R, Bansmann J, Leupold O and Meiwes-Broer K H 2003 *New J. Phys.* **5** 47
[79] Maaz K, Mumtaz A, Hasanain S K and Bertino M F 2010 *J. Magn. Magn. Mater.* **322** 2199
[80] Li Z, Xie Y, Yuan Y, Wang M, Xu C, Hübner R, Prucnal S and Zhou S 2021 *J. Magn. Magn. Mater.* **532** 167981
[81] Wäppling R and Häggström L 1968 *Phys. Lett.* A **28** 173
[82] Streubel R, N'Diaye A T, Srinivasan K, Ajan A and Fischer P 2019 *Appl. Phys. Lett.* **114** 162401
[83] Woltersdorf G and Heinrich B 2004 *Phys. Rev.* B **69** 184417
[84] McMichael R and Krivosik P 2004 *IEEE Trans. Magn.* **40** 2–11
[85] Lenz K, Wende H, Kuch W, Baberschke K, Nagy K and Jánossy A 2006 *Phys. Rev.* B **73** 144424
[86] Arias R and Mills D L 1999 *Phys. Rev.* B **60** 7395
[87] Nguyen N *et al* 2023 *J. Phys.: Condens. Matter* **35** 485801
[88] Kittel C 1948 *Phys. Rev.* **73** 155–61
[89] Farle M 1998 *Rep. Prog. Phys.* **61** 755
[90] Van Vleck J H 1950 *Phys. Rev.* **78** 266
[91] Shaw J M *et al* 2021 *Phys. Rev. Lett.* **127** 207201
[92] Chen C T, Idzerda Y U, Lin H J, Smith N V, Meigs G, Chaban E, Ho G H, Pellegrin E and Sette F 1995 *Phys. Rev. Lett.* **75** 152
[93] Thole B T, Carra P, Sette F and van der Laan G 1992 *Phys. Rev. Lett.* **68** 1943–6
[94] Carra P, Thole B T, Altarelli M and Wang X 1993 *Phys. Rev. Lett.* **70** 694–7
[95] van der Laan G and Figueroa A I 2014 *Coord. Chem. Rev.* **277-278** 95
[96] Pahari R *et al* 2021 *Phys. Rev. Mater.* **5** 124418
[97] Streubel R, N'Diaye A T, Srinivasan K, Kalitsov A, Jain S, Ajan A and Fischer P 2021 *J. Phys.: Condens. Matter* **33** 104003
[98] Streubel R, Köhler D, Schäfer R and Eng L M 2013 *Phys. Rev.* B **87** 054410
[99] Teague M R 1983 *J. Opt. Soc. Am.* **73** 1434
[100] Streubel R 2023 *J. Mater. Res.* **38** 4977
[101] Kravchuk V P, Sheka D D, Streubel R, Makarov D, Schmidt O G and Gaididei Y 2012 *Phys. Rev.* B **85** 144433
[102] Kravchuk V P, Rößler U K, Volkov O M, Sheka D D, van den Brink G, Makarov D, Fuchs H, Fangohr H and Gaididei Y 2016 *Phys. Rev.* B **94** 144402

[103] Tanaka G, Yamane T, Héroux J B, Nakane R, Kanazawa N, Takeda S, Numata H, Nakano D and Hirose A 2019 *Neural Netw.* **115** 100
[104] Sutton M, Mochrie S G J, Greytak T, Nagler S E, Berman L E, Held G A and Stephenson G B 1991 *Nature* **352** 608
[105] Seaberg M H *et al* 2017 *Phys. Rev. Lett.* **119** 067403
[106] Burn D M, Zhang S L, Wang S, Du H F, van der Laan G and Hesjedal T 2019 *Phys. Rev.* B **100** 184403
[107] Shpyrko O G *et al* 2007 *Nature* **447** 68
[108] Sinha S K, Jiang Z and Lurio L B 2014 *Adv. Mater.* **26** 7764
[109] Néel L 1949 *Ann. Geophys.* **5** 99
[110] Brown W F 1963 *Phys. Rev.* **130** 1677
[111] Vogel H 1921 *Phys. Z.* **22** 645
[112] Fulcher G S 1925 *J. Am. Ceram. Soc.* **8** 339
[113] Tammann G and Hesse W 1926 *Z. Anorg. Allg. Chem.* **156** 245